

<https://doi.org/10.1038/s41699-024-00457-w>

Microwave graphitic nitrogen/boron ultradoping of graphene



Rebti Bhushan¹, Arkamita Bandyopadhyay², Sangeeth Kallatt^{3,4}, Awalendra K. Thakur¹, Swapan K. Pati⁵ & Prashant Kumar^{1,6} ✉

Insufficient carrier concentration and lack of room temperature ferromagnetism in pristine graphene limit its dream applications in electronic and spintronic chips. While theoretical calculations have revealed that graphitic ultradoping can turn graphene into semiconducting and room temperature ferromagnetic, the exotic set of thermodynamic conditions needed for doping result in defects and functionalities in graphene which end up giving significant electronic scattering. We report our discovery of microwave ultradoping of graphene with N > 30%, B ~ 19%, and co-doping to form BCN phases (B₅C₇₃N₂₂, B₈C₇₆N₁₆, and B₁₀C₇₇N₁₃). An unprecedented level of graphitic doping ~95% enhances carrier concentration up to $\sim 9.2 \times 10^{12} \text{ cm}^{-2}$, keeping high electronic mobility $\sim 9688 \text{ cm}^2 \text{ V}^{-1} \text{ s}^{-1}$ intact, demonstrated by field effect transistor measurements. Room temperature ferromagnetic character with magnetization $\sim 4.18 \text{ emu g}^{-1}$ is reported and is consistent with our DFT band structure calculations. This breakthrough research on tunable graphitic ultradoping of 2D materials opens new avenues for emerging multi-functional technological applications.

Atomically thin mono-elemental sheets including graphene^{1–4} (sp²-hybridized atomic sheet of carbon), phosphorene⁵, silicene⁶, borophene^{7–12}, two dimensional (2D) gold¹³, berylline¹⁴, molybdenene¹⁵ etc. are collectively termed as Xenes and they exhibit Dirac or Dirac-like behavior. Apart from Xenes¹⁶, transition metal dichalcogenides (TMDCs)¹⁷, transition metal oxides (TMOs)¹⁸ and transition metal carbide/nitride/carbonitrides (MXenes¹⁹) and several other materials which have been obtained in the form of flat atomic sheets broadly constitute 2D materials, each exhibiting unique set of physical/chemical properties. These advanced quantum materials boast high surface area, surface anchoring capability via π - π interactions, coupled with world-record electronic mobility, excellent thermal conductivity and tremendous 2D/3D stretching capabilities, making them the most popular class of materials for their applications in FET/SERS based molecular/gas/chemical ultrafast sensing, hydrogen/halogen storage, excitonics, as a UV shield, in thermal interfacing, and electronic, photonic, thermal as well as mechanical metamaterials^{20–29}. Apart from myriads of consumer products, graphene, the first member of the family of 2D materials has extensively been implemented large scale industrial scale applications, e.g., in civilian architectures, aeronautical components, anti-

corrosive coating in ships etc. and thus it has been inspiring discoveries of new 2D materials, and innovative futuristic technologies.

The dream of realizing graphene-based coveted fast and flexible electronic as well as spintronic chips still remains elusive due to insufficient carrier concentration, and an ambivalent and nonmagnetic nature of graphene in its pure form³⁰. Even though field doping, molecular charge transfer, ion bombardment, functionalization, etc. can create charge-/spin-asymmetry in graphene, heteroatom substitutional doping is promising for intrinsic qualities^{31,32}. Most of the reported literature however speaks about edge/surface non-graphitic doping^{33–35}. While in-situ doping by chemical vapor deposition (CVD) results in inadequate (<10%) doping, fluorination-defluorination-thermal doping³⁶ resulted in high (~30%) doping primarily (>75%) non-graphitic. Most of these doping techniques are usually multi-step synthesis, cumbersome, involve uncontrollable reactions, and often end up in fragmenting graphene sheets apart from defect/vacancy generation and enhanced oxygen content in the system³⁷. Moreover, these techniques suffer from scalability and tunability issues as well. Attempts to enhance dopant % usually end up with curtailing graphitic content. In brief, precisely tunable significant-level graphitic doping of graphene in a controlled

¹Department of Physics, Indian Institute of Technology Patna, Patna, Bihar 801103, India. ²The Bremen Center for Computational Materials Science (BCCMS), Universität Bremen, Am Fallturm 1, TAB Building, 28359 Bremen, Germany. ³Centre for Nano Science and Engineering (CeNSE), Indian Institute of Science, Bengaluru 560012, India. ⁴Niels Bohr Institute, University of Copenhagen, 2100 Copenhagen, Denmark. ⁵Theoretical Sciences Unit, Jawaharlal Nehru Centre for Advanced Scientific Research, Bengaluru 560064, India. ⁶Global Innovative Centre for Advanced Nanomaterials, University of Newcastle, Callaghan Campus, Newcastle, NSW 2308, Australia. ✉ e-mail: Prashant.Kumar@newcastle.edu.au; magmemory@gmail.com

manner has not yet been attained. This technological gap has been the bottleneck for technological advances toward targeted applications.

Gauging the urgency of graphitic ultra-doping in graphene to equip it for electronic and spintronic chip applications, we employed purely microwave power as an external energy source for ultradoping of graphene (details in the method section). We analyzed microwave synthesized materials for their crystal structures, doping type, and the level of doping by employing high-resolution transmission electron microscopy (HRTEM) as well as spectroscopies (Raman, X-ray photoelectron (XPS) and Fourier transform infrared (FTIR)). Spin-polarized DFT band structure calculations were carried out for doped systems to theoretically assess the electronic and magnetic character of heteroatom-doped graphene systems. We fabricated field effect transistor (FET) devices with doped graphene as active materials (details in the method section) to investigate Dirac point modulation (if any) and also to explore carrier enhancement upon doping. To explore magnetic ordering caused by graphitic ultra-doping, a vibrating sample magnetometer (VSM) was employed for attaining M Vs H hysteresis loop and for field cooled-zero field cooled (FC-ZFC) magnetization vs temperature (M - T) data.

Results and discussion

In the realm of graphene applications, electronic-spintronic 2D-transistor applications stand out, driven by graphene's intrinsically excellent carrier mobility; however, the full potential of this application is hindered by insufficient carrier concentration, inadequate transconductance, and the absence of room temperature ferromagnetism. Therefore, achieving charge- and spin-asymmetry is crucial for the charge-spin 2D FET application. The viable practical method to accomplish charge and spin asymmetry in otherwise ambivalent graphene is heteroatom doping. Graphitic (sp^2)

incorporation of dopant can bring asymmetries with the minimal extent of electronic scattering thereby keeping the mobility intact. Unlike magnetism arising from edges, functionalities, or non-graphitic doping, which is extrinsic and results in Curie point below room temperature, graphitic ultradoping becomes a prerequisite for future-generation carbon electronics and spintronics. Traditional doping techniques suffer from uncontrollable tear (C-C bond breaking) and very slow repair (C-N or C-B bond formation) mechanisms. In contrast, MW doping involves controlled tear and prompt repair which enables MW tremendous potential for performing heteroatom doping efficiently, promptly, and most importantly graphitically^{38–40}.

Synthetic protocols for N/B doped graphene sheets

In this article, pristine undoped few layers CVD graphene is referred to as FLG. N-doped and B-doped samples synthesized at 850 W are named NG850 and BG850 respectively. Similarly, NG720, NG640, NG560, NG480, BG720, BG560, and BG480 were attained at corresponding power levels. BNG1, BNG2, BNG3, BNG4, BNG5, BNG6, and BNG7 correspond to N-, B-co-doped systems; all synthesized at the same MW power but at distinct combinations of B/N precursor ratios (wt.%) e.g., 0.43, 0.66, 1.00, 1.22, 1.5, 1.85 and 2.33 (see synthesis parameter details in Supplementary Table 1 and ESI). FLG being semi-metallic, absorbs microwave and triggers microwave plasma⁴¹ (see Supplementary Fig. 1), generating hot spots at the interface of FLG and doping precursors, which raises the local temperature beyond 2000 °C. Akin to excimer laser processing reported earlier³⁹, elevated temperature facilitates vacancy formation in the basal plane of FLG. Localized thermal spikes are also responsible for the breaking of bonds of doping precursor. Schematic diagrams for the mechanism of N-, B- and co-doping of FLG at the Basal plane are shown in the first column of Fig. 1. In contrast to

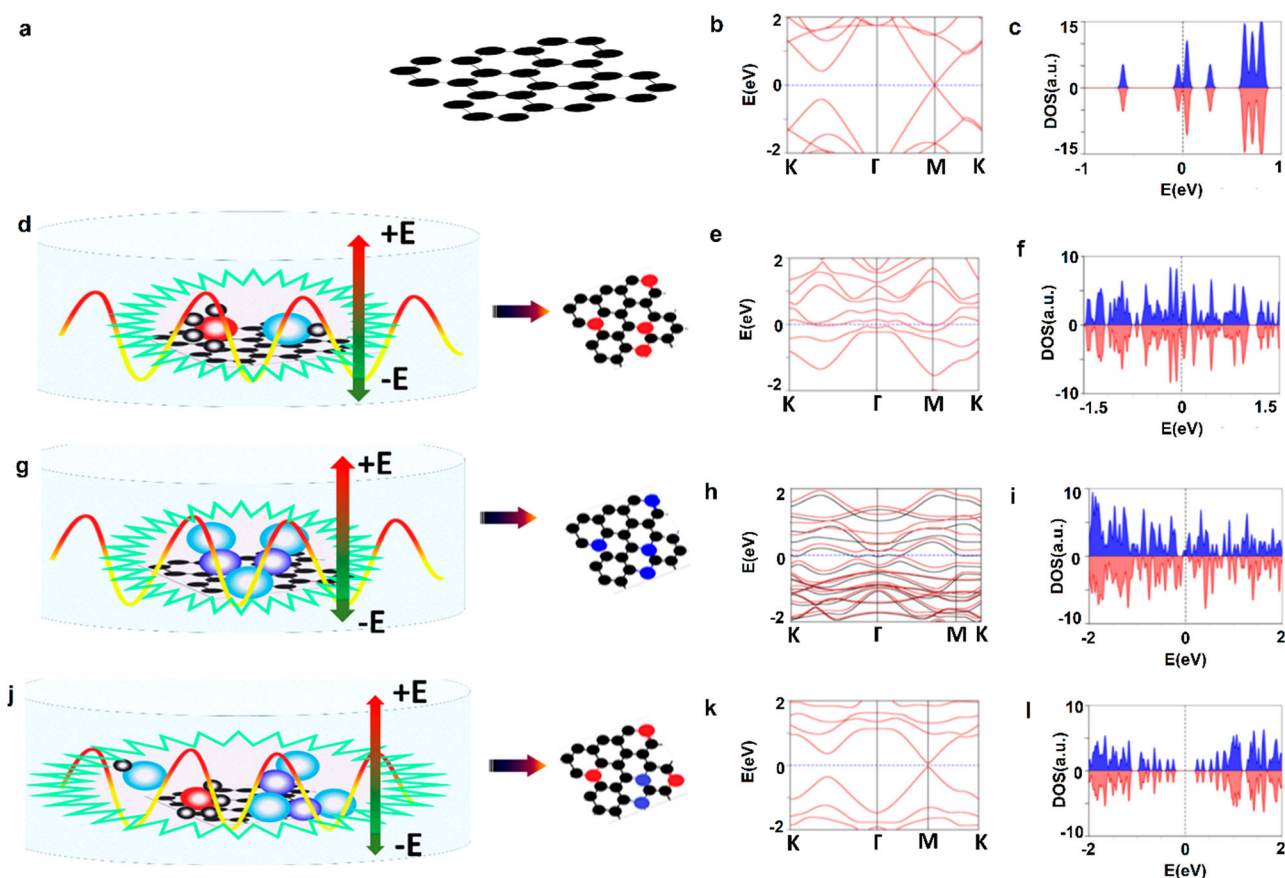


Fig. 1 | Synthetic protocols and density functional theory. a sp^2 hybridized hexagonal graphene lattice (pristine sample). Schematic diagram (1st column) for microwave graphitic ultradoping of graphene (d) by N using NH_4OH as nitrogen precursor, (g) by B using B_2O_3 as boron precursors and (j) N, B co-doping by using

NH_4OH and B_2O_3 simultaneously (red: nitrogen atom, black: carbon atom, blue: boron atom). DFT band structure and DOS (2nd and 3rd column) for (b, c) graphene, (e, f) N-doped graphene, (h, i) B-doped graphene and (k, l) N, B co-doped graphene.

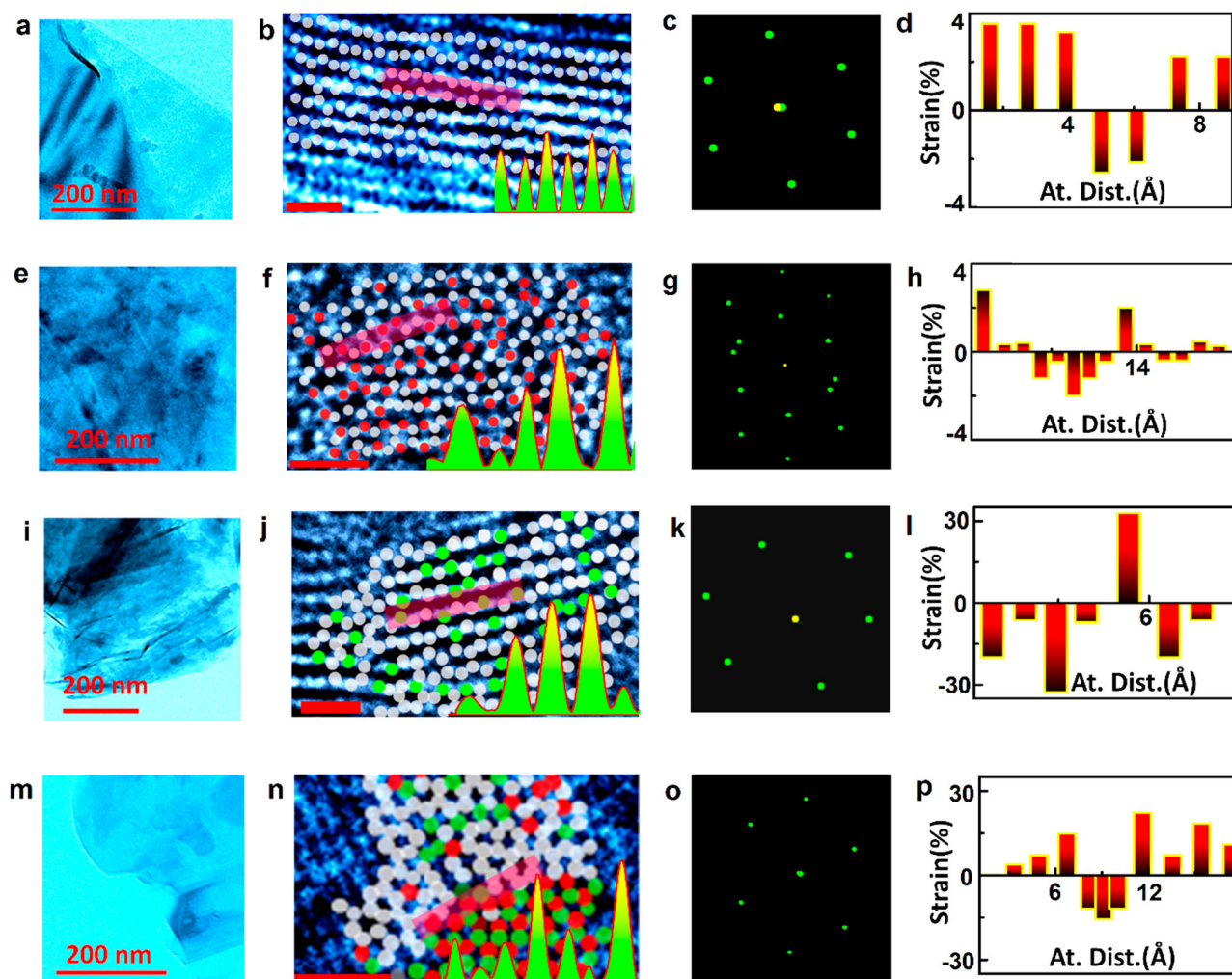


Fig. 2 | Transmission electron microscopy. Large area TEM images (first column), selected area atomic resolution TEM images as well as the atomic profile of selected areas (second column), FFT patterns of selected area atomic images (third column),

and strain profiles obtained from HRTEM images (fourth column) for (a–d) FLG, (e–h) NG720, (i–l) BG720 and (m–p) BNG3.

conventional doping, predominantly driven by thermal diffusion, MW doping is predominantly electric field driven^{42,43}. It should be noted that the field-driven phenomena are quite common in thin film systems and atomically thick graphene would even be more vulnerable^{44,45}. As the supplied energy i.e., the electric field can externally and precisely be tuned, the MW-doping technique provides precision in doping level. Contrary to existing conventional doping techniques with lower product yields, the MW-doping technique efficiently enables batch doping, yielding ~733 mg of doped product in just ~600 s boasting an impressive yield of ~61% (calculated in terms of doping precursor). Detailed scalability parameters and results are given in Supplementary Table 1 and Supplementary Fig. 2a–d.

DFT band structure calculation of N/B doped graphene sheets

DFT band structure calculations and DOS (2nd and 3rd column in Fig. 1 and Supplementary Fig. 4a–d) reveal that graphitic doping induces smaller band gap(s) ~100 meV. Graphitic doping introduces less disturbing desirable defects, preserving the sp^2 cloud and ballistic mobility intact, therefore, its contribution to bandgap opening is smaller. Conversely, pyridinic/pyrrolic doped graphene exhibited a band gap of ~300 meV, and BNG1 demonstrated a significantly larger calculated value of ~0.6 eV (see Supplementary Fig. 3a–c) for lattice consideration). It's important to note that DFT calculations tend to underestimate band gaps. While FLG has energy levels uniformly distributed below and above the Fermi level, NG720 and BG720 exhibited a higher number of lines above and below the Fermi level

respectively suggesting n-type and p-type carrier doping, also confirmed by charge density difference profile (see Supplementary Fig. 5). Interestingly, upon resolving up-spin and down-spin DOS, we could vividly conclude that while non-graphitic (pyridinic/pyrrolic) doping leads to higher magnetization^{31,46}, graphetically doped samples may not exhibit high magnetization, however, high Curie point is expected.

Atomic resolution imaging by HRTEM

TEM images for FLG, NG720, BG720, and BNG3 are shown in 1st column of Fig. 2. Electron imaging unveils that doped graphene sheets are 500 nm–2 μ m in lateral dimension and predominantly exhibit 1–2 layers, apparent from electron transparency as well as the presence of ripples and folds. MW irradiation facilitates the exfoliation of layers as well. Uniform electron transparency hints at uniform dopant incorporation via the MW method. Atomic resolution HRTEM images (see 2nd column of Fig. 2) exhibit hexagonal atomic structure in all the cases with atomic contrast variation, confirming the substitution of heteroatom dopant into the basal plane of graphene lattice. A comprehensive understanding and insight into dopant placement and distribution is indexed in HRTEM images at atomic resolution. Atomic placements have also been integrated and validated with elemental analysis results via XPS. Apparent from FFT patterns (see Fig. 2, 3rd column), as compared to FLG which exhibits a hexagonal pattern with crystallographic dots making ~120° angle at vertices; doped samples exhibit altered lattice constants and bond angles attributed to heteroatom substitution. While FLG exhibited

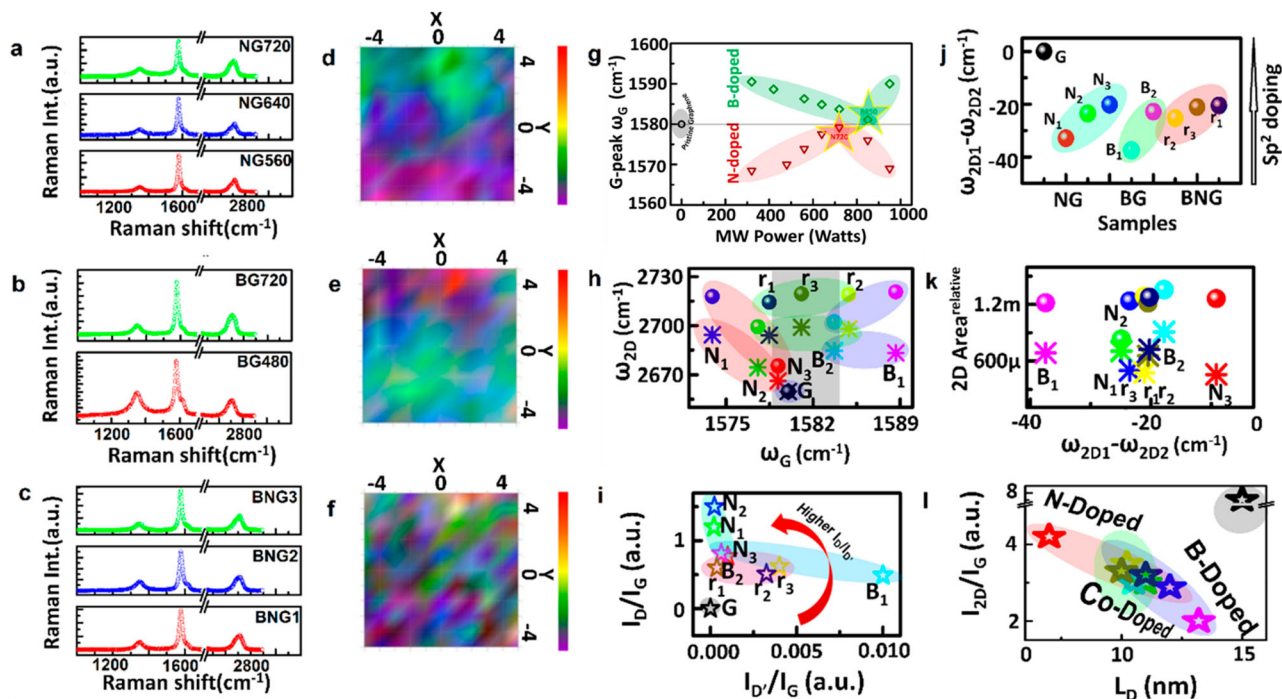


Fig. 3 | Raman spectroscopy. Raman spectra for (a) N-doped, (b) B-doped, and (c) B-N-doped graphene samples synthesized at various MW powers. Raman mapping for G peak spectral variation in doped graphene system for (d) N720, (e) B720, and (f) BNG3 w.r.t G peak of FLG (1580 cm^{-1}) for an area of $10\text{ }\mu\text{m} \times 10\text{ }\mu\text{m}$. (Color code —Yellow: 1580 cm^{-1} , Red: $+15\text{ cm}^{-1}$, Violet: -15 cm^{-1}). Raman spectra analysis for

doped graphene samples with FLG: Plots for (g) shift in G peak frequency of synthesized samples w.r.t FLG at various MW power, (h) ω_{2D} vs ω_G , (i) Intensity ratio of D and G vs Intensity ratio of D' and G, (j) $\Delta\omega$ for $2D_1$ and $2D_2$ peaks for all samples, (k) Relative area vs $\Delta\omega$ for $2D_1$ and $2D_2$ peaks, (l) Intensity ratio of 2D and G vs L_D .

mostly compensated strain, NG720, BG720, and BNG3 exhibited uncompensated strain (see Fig. 2, 4th columns). In general, N-doping tends to induce uncompensated tensile strain and B-doping induces uncompensated compressive strain. However, the specific effect on the alteration of bond length and bond angle depends on the dopant configuration.

Graphitic doping configuration causes minimal distortion in lattice parameters hence expected to keep the electronic mobility intact. Whereas non-graphitic doping tends to affect bond length to the larger extent. In the case of BNG3, we obtained BN patch formation which relaxes lattice strain. Strain patterns attest to the reflex action of graphene against doping. Uncompensated strain evolves if one tries to heavily dope and such samples having high carrier density exhibit altered band structure which has been confirmed by DFT calculations. NG720 exhibited minimum uncompensated tensile strain i.e., $< 4\%$. BNG3 exhibited the formation of BN patches with surprisingly elongated and sheared hexagons in the FFT pattern, indicative of N-B-N and B-N-B bonds. Atomic profiles for C, B, and N all together (see Fig. 4f mixed color) and those for individual atoms i.e., for C, B, and N (in green, red, and blue respectively) for BNG3 demonstrate the uniformity of doping and co-existence of B and N. One can easily make out almost equal percentages of B and N, further confirmed by XPS. TEM analysis and DFT calculations indicate that localized atomic level strains as well as electrostatic charge density both act simultaneously in doped graphene systems and determine their final electronic band structures.

Chemical phase confirmation by Raman spectroscopy

Raman analysis is a versatile tool to get insights into the incorporation of dopants into the graphene lattice. The MW power-dependent variation in spectra for B-, and N-doped graphene samples and B/N precursor ratio-dependent variation for BN co-doped samples are shown in Fig. 3a–c. The extent and the configuration of the dopant affect the bond length and induce strain in the hexagonal lattice which alters the position of the G-peak band. Shift in the G-peak band which is a first-order Raman active mode, upon doping, is mainly caused by electron-dopant elastic scattering and electron-

phonon inelastic scattering. We observed, B-dopants bestow a downshift in G-band frequency and N-dopants bestow an upshift in G-band frequency (Fig. 3g). N-atom donates an electron to the hexagonal matrix and creates electron electron-dense cloud which increases the bond length whereas B-atom takes one electron away from the sp^2 cloud of graphene resulting in a decrease in the bond length. Moreover, the extent of electron cloud redistribution depends on the configuration of bonding. Furthermore, the extent of G-band shift depends on how destructive the nature of the dopant is. More defective doping is sp^3 and sp doping configurations which disturb the sp^2 symmetry of graphene and cause large deviation in G-band position. However, graphitic (sp^2) doping is a minimal defective doping configuration that preserves the ballistic sp^2 cloud of graphene lattice. The deviation in the G-band again started increasing after reaching the maximum threshold for graphitic content in N720 and B850. Therefore, the incorporation of dopant into the matrix beyond threshold limits undermines the structural stability⁴⁷.

As Raman spectra have overall information embedded in them, it does not reveal intricate local details about doping distribution, and therefore, Raman mapping was carried out for G peak for $10\text{ }\mu\text{m} \times 10\text{ }\mu\text{m}$ (see Fig. 3d–f). One can easily observe that NG720 shows graphitic n-type doping as evident from the softening of the G-peak and a kind of non-graphitic p-type doping in BG720 as evident from stiffened G peak. It is well known that Raman mapping having poor resolution, can't reveal exact atomic scale information and therefore we could not attain direct mapping of BN patches. However, TEM and HRTEM resolved it well and moreover, BN patches were electron opaque. Also, we could see a network of softened and stiffened G modes in Raman mapping for BNG3 sample (Fig. 3f) attributed to the embedded BN patch in the hexagonal lattice. Splitting in 2D peak ($2D_1$ and $2D_2$) for graphitic ultradoped samples, obtained upon deconvolution may arise due to defects, doping, or stacking. In general, high MW power leads to the higher graphitic extent and undergoes minimal 2D peak splitting, and in contrast, low power results in higher 2D peak splitting which signifies non-graphitic doping (see Fig. 3h, j, k).

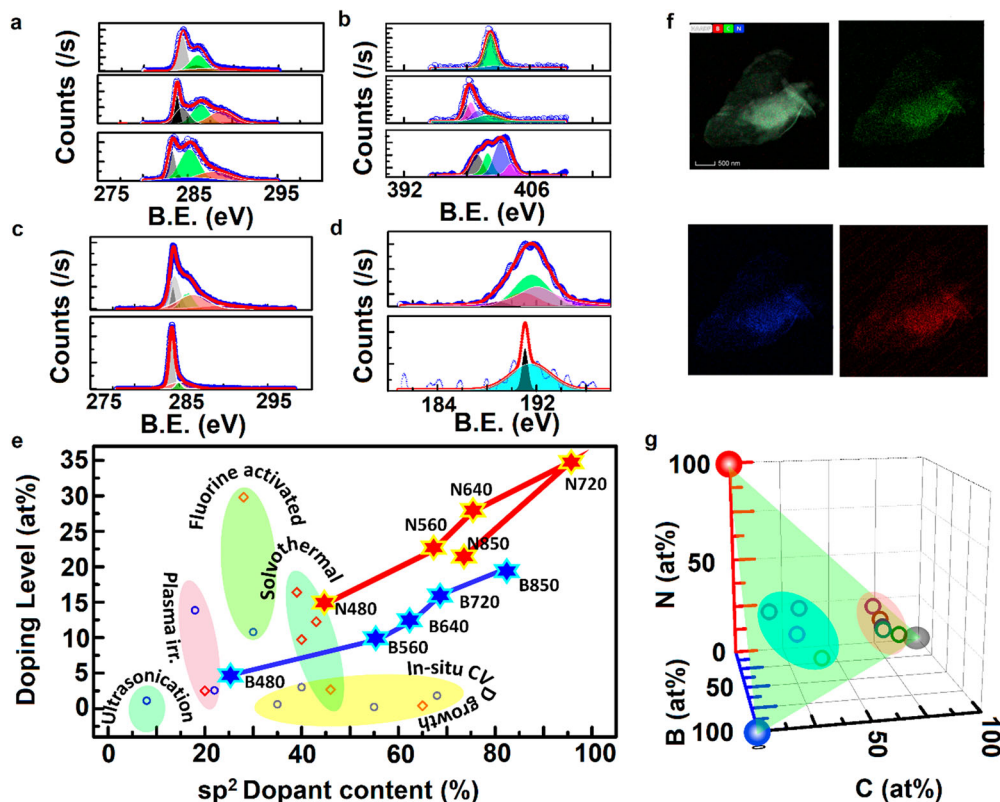


Fig. 4 | X-ray photoelectron spectroscopy. XPS spectra for (a) C 1 s and (b) N 1 s peaks for N-doped graphene synthesized at various microwave power levels, (c) C 1 s and (d) B 1 s peaks for B-doped graphene synthesized at various microwave power levels. e Plot depicting trend of Graphitic % vs Doping % for doped graphene samples achieved at various microwave power (present report) along with those for doped graphene systems in literature such as for in-situ CVD growth, plasma treatment,

Pyrolysis and fluorine activated followed by doping^{15,29–32,39,40}. The doping level as well as graphitic % is the best in microwave N720 (theoretical limit ~33% sp² incorporation achieved) and B850. f Atomic profile for all three atoms C, B and N together (Mixed color), only carbon (green color), only boron (red color) and only nitrogen (blue color) for BNG3. g 3D diagram of atomic % showcasing various phases of BCN attained at different B/N precursor ratio (from present report) and literature⁵¹.

One cannot exceed the theoretical graphitic doping limit⁴⁷, therefore, NG850 (see Supplementary Table 1) exhibited a more non-graphitic nature than NG720. In contrast to C and N, the atomic size of B is large, and its electronegativity is less compared to N. Therefore, the energy needed for graphitic B doping is higher than that for N. In fact, we did see some glimpses of it. While NG 850 is partially non-graphitic, BG850 exhibited a predominately graphitic nature (see Supplementary Table 1). The relative area of the 2D₂ peak decreases as the microwave power is increased and simultaneously relative peak area for 2D₁ increases (see Fig. 3k) and such trends are characteristic of improved graphitic nature^{48,49}. In the case of co-doping with a number of BCN phases, BNG1 has higher N doping which is graphitic and BNG3 has graphitic doping (equal precursor ratio resulted in BN patch formation). Thus, graphitic doping generally manifests a 2D₂ sub-peak with reduced intensity and minimal peak splitting in the deconvoluted 2D peak for graphitic-doped samples compared to non-graphitic doping. Further, high MW power synthesized samples (e.g., NG720) have exhibited lower I_D/I_G ratio and reverse is true for low MW power case, suggesting higher sp³ content and hence non-graphitic doping in the latter case (see Fig. 3l). It should be noted that I_D would not alter for graphitic doping which keeps lattice intact, and it has been observed in the present work too. Estimation of defect density length (see Fig. 3l) is derived from the modified local activation model⁵⁰. M.M. Luchese model that relates the evolution and alteration of defect peaks (D peak and D' peak) and broadening in 2D peak with average inter-defect distance L_D. The function is described below.

$$\frac{I_{2D}}{I_G}(L_D) = \frac{I_{2D}}{I_G}(FLG) - B \left[1 - \exp\left(-\frac{\pi r_s^2}{L_D^2}\right) \right] \quad (1)$$

The estimation of activation constant B is done at a laser 514 nm (E_{laser} = 2.14 eV). This model has been fitted for unit activated area r_A = 1 nm² over a sheet area 50 nm X 50 nm by considering the point defect to be a dopant with a structural area r_s = 0.156 nm² per dopant. It reveals meaningful information related to doping sites (graphitic/non-graphitic) in graphene which is a function of MW power as the sole control parameter in the case of elemental doping and a function of both precursor ratio and MW power in the case of multi-component doping. The defect density length is a parameter that reflects the spatial distribution of dopants within a given length scale. It is an inter-defect length. Analyzing the ratio of disorder-induced band intensity (integrated area ratio) with G-band provides insight into the distribution of dopants. While FLG has L_D ~ 15 nm, NG720 exhibited L_d ~ 4 nm, which is a record in itself. Similarly, BG850 also exhibited ~8 nm which is lower than that for FLG. In contrast, BNG samples are closely spaced w. r. t. FLG in I_{2D}/I_G vs L_D plot. The estimated value of L_D in this case is very large ~12.4 nm attributed possibly to BN patch formation. Since L_D quantifies defect concentration which gives blanket information and includes vacancies and doping, a reduction in L_D may not give conclusive information as to whether the change in its value arises due to doping, or vacancy formation during synthesis.

Evaluation of extent and nature of doping by XPS

To get exact confirmation regarding it, we have carried out the XPS analysis. Upon deconvolution of C 1 s peak, NG540, NG640, and NG 850 resulted in sub-bands of C = C stretch (~284 eV) and revealed partial sp³ nature of the C-C bond which attests to non-graphitic and edge doping. Interestingly though, NG720 did not exhibit such sp³ behavior (see Fig. 4a). NG720 exhibited N-doping (band at 285.3–285.9 eV) with an insignificant peak at 287.2 eV which confirms minimal oxygen functionality. Upon

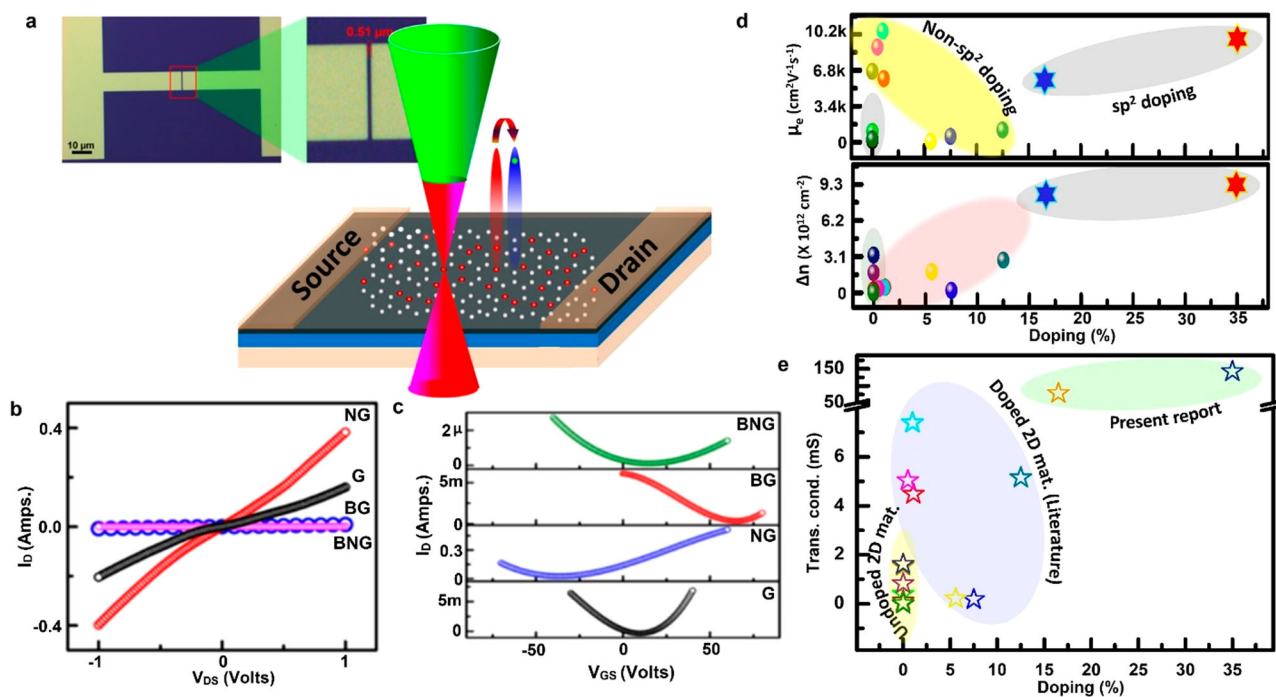


Fig. 5 | FET characterization. **a** Optical imaging and schematic of FET device with doped graphene system as the channel, **(b)** output characteristics (I_{DS} vs V_{DS}) and **(c)** transfer characteristics (I_{DS} vs V_{GS}) for G i.e., FLG, NG i.e., NG720, BG i.e., BG720 and BNG i.e., BNG3. **d** Literature comparison plot depicting effective carrier concentration injected after doping and effect on their majority charge carrier mobility

(doping) (%) = 0 i.e., pristine 2D materials such as silicene, phosphorene, MoS₂, CNT and GNR^{2,4,21,36,37,69–73} and **(e)** transconductance vs. Doping % depicting overall electromigration transport capability comparison of present report systems with various 2D pristine and doped systems from literature^{2,21,69–74}.

deconvolution of N1s fine spectra, NG540, NG640, and NG850 exhibited peak ~398 eV (pyridinic), ~399–400 eV (pyrrolic), and a peak ~401 eV (graphitic) (see Fig. 4b). In contrast, NG720 exhibited only graphitic and no pyridinic or pyrrolic peaks. Moreover, minimal sub-bands at 402.76 and 403.96 eV which appear for N-O functionality; is completely absent in NG720. N-doping was calculated to be ~14.9%, ~22%, ~28%, ~35% and ~22.8% for N480, NG560, NG640, NG720, and NG850 respectively. Oxygen content for NG720 and NG850 was minimal as compared to those synthesized at lower powers. Upon precise doping nature evaluation, pyrrolic % were ~28%, ~10.3%, ~11.6%, ~1.5%, and ~25%, pyridinic % were ~27%, ~17.7%, ~13.4%, ~3.5% and ~7% and most importantly graphitic % were ~45%, ~72%, ~75%, ~95% and ~68% for NG480, NG560, NG640, NG720 and NG850 respectively. Such a high nitrogen doping level especially graphitic extent with insignificant oxygen functionalities at 720 W microwave power; is claimed to be a breakthrough result not yet reported. Doping as well as graphitic percentage along with negligible oxygen content in microwave synthesized samples in the present report is superior to any prior report in the existing literature (see Fig. 4e).

Boron doping is often difficult as apart from the atomic size and electronegativity factor, high energy is needed to break bonds in solid precursor; the B-doping record till date is ~11%. Upon deconvolution of C 1s spectrum of BG720, we attained sub-bands at 284.4, 284.9, 287.4 eV which correspond to C=C, C-B and C-O respectively (see Fig. 4c). BG480 exhibited a sub-peak at ~289.9 eV (C=O) in addition to the three peaks observed for BG720. When B1s fine spectra of BG720 was deconvoluted, we attained sub-peaks at 188.9, 190.9, 191.6 and 192.5 eV (see Fig. 4d). While the first three sub-peaks correspond to C₃B bonding i.e., sp² doping of boron, the last peak at 192.5 eV corresponds to C₂B-O bonding i.e., boronic type, a non-graphitic nature. In our case, B₂O₃ was used as a precursor, which often gives a peak at 194.12 eV and we could not get any signature of B₂O₃ in XPS spectra. This confirmed that there is no residual precursor in the product. Further, no signature of higher oxygen functionality such as boronic (B-CO₂) could be seen. While peak analysis of BG720 confirmed

~16% boron doping out of which 68% is graphitic. Interestingly enough, BG850 in particular exhibited ~19.8% B-doping out of which 82.6% is graphitic, which sets a new record for B atom incorporation in graphene. Microwave power tunability of B-doping level has also been achieved. In summary, an increase in microwave power correlates with elevated doping levels and graphitic content until the theoretical limit, decreasing thereafter (Fig. 4e). Graphitic doping exhibits a lower oxygen extent than non-graphitic doping. We also confirm that at low microwave power, more destructive doping i.e. edge doping and non-graphitic doping prevails, while higher power favors graphitic doping and the sp² cloud of graphene remains intact. Less destructive dopant incorporation enhances carrier concentration while keeping charge transport mobility intact.

The synthesis strategy adopted also yielded several BCN phases. The final B/N ratios in synthesized co-doped systems are B₅C₇₃N₂₂, B₈C₇₆N₁₆, and B₁₀C₇₇N₁₃ phases of BCN (see Fig. 4g and Supplementary Fig. 6)⁵¹. As is apparent from the G-peak shift and XPS analysis, sp² hybridization in these BCN phases remains intact. Since there is an immense freedom of selection of B/N ratio, one can; therefore, tune the electronic and excitonic behavior of graphene by co-doping it with desirable doping levels. Co-doped graphene for particular ratios will result in BCN phases.

Field effect transistor measurements

The dopant percentage and in-plane distribution in FLG determine net injected carrier concentration and electromigration characteristics, which in turn would influence the overall mechanism of electronic transport in devices. Field effect transistors (FET) were therefore fabricated employing EUV lithography, optical image of electrodes, and schematic of FET device in Fig. 5a, with doped graphene samples implemented as active material. The fabricated device features a channel length of ~0.5 μm and a channel width of 10 μm on 100 nm of thermally oxidized silicon surface on silicon substrate (device fabrication details in method section). The output and transfer characteristics are analyzed to assess the difference in the impact of graphitic and non-graphitic incorporation of dopants in graphene.

Moreover, the results also validated the trend of concentration and type of induced charge carriers due to doping and the extent of charge localization associated with various doping sites.

Output characteristics (I_{DS} vs V_{DS}) for NG720, BG720, and BNG3 revealed semi-metallic conducting behavior, (see Fig. 5b), with NG720 demonstrating excellent electromigration capabilities at room temperature. It is worth noting that NG720 exhibited superior electronic transport performance with enhanced drain current $I_{DS} \sim 2.3$ times higher than FLG, primarily attributed to in-plane graphitic ultradoping. However, non-graphitic doping samples exhibited curtailed transport behavior under the same gate potential due to non-graphitic contents acting as scattering centers for carrier mobility. A relatively lower drain current than NG720 in BG720 (10 mA) and BNG3 (0.67 mA) confirms the charge carrier localization effect due to non-sp² doping configuration. Therefore, graphitic incorporation of dopant is a prerequisite for superior in-plane electromigration. Furthermore, the transfer characteristics are analyzed to gain insights into electron-hole symmetry breaking accompanying ultradoping and underlying transport mechanisms. Interestingly, NG720 and BG720 exhibited a significant shift in Dirac point, ~ -40 V and ~ -60 V respectively, from ambivalent FLG (~ 10 V) which confirms resultant electron-hole asymmetries and injection of carrier n-type and p-type respectively. Doped samples exhibited different slopes on either side of the Dirac point, representing dopant-induced asymmetries and dissimilar electron, μ_e , and hole, μ_h , mobilities.

BG720, with partial edge doping, showed a larger Dirac shift than the graphitically doped NG720 (see Fig. 5c), experimentally aligning and authenticating with the theoretical prediction (DFT calculation) of opening larger band gaps in non-graphitically doped graphene systems than graphitically doped graphene systems (see 3rd and 4th column of Fig. 1, and Supplementary Fig. 4). Despite opening larger band gaps, non-graphitic content compromised carrier mobility and degraded transport capability. NG720 exhibited enhanced electronic mobility (~ 9688 cm²V⁻¹s⁻¹) and higher effective carrier concentration ($\sim 9.2 \times 10^{12}$ cm⁻²). Moreover, ultimate graphitic content in NG720 attributes a steep subthreshold slope, a smaller threshold swing (2.2 times smaller than BG720 and 3.7 times smaller than BNG3), and an enhanced I_{ON}/I_{OFF} current ratio. Non-sp² content, attributes curtailed electronic mobility (~ 5903 cm²V⁻¹s⁻¹) in BG720. Carrier mobility degrades in BNG3 due to BN patch formation. The excellent transport performance of FET devices is attributed to higher Δn (net majority carrier concentration). Record level, viz., $\sim 9.2 \times 10^{12}$ cm⁻² and 8.3×10^{12} cm⁻² for NG720 and BG720 respectively, of Δn among carbon-based materials are attributed to ultradoping in general and the graphitic nature in particular (see Fig. 5d). NG720 exhibited the highest transconductance ($\mu\Delta n$) ~ 142 mS, setting a new record for graphene-based systems and 2D materials in general, as illustrated in Fig. 5e. Significantly large majority carrier concentration and mobility attributes excellent drain current at minimal V_{DS} showcasing its potential for low-power electronic device applications.

Magnetic measurements

While spin-interactions are responsible for magnetic ordering, spin-fluctuations caused by thermal effect lead to randomization^{52–55}. The temperature is a critical factor in determining magnetic order, and materials undergo transitions to paramagnets above Curie point⁵⁶. In 3D crystalline itinerant ferromagnetic materials, T_c is indicative of magnetic ordering⁵⁷. Single crystal sp-electron-only graphene sheet is non-magnetic in its pure form⁵⁸. However, dangling bonds at edges create active paramagnetic centers, rendering pristine graphene mildly magnetic⁵⁹. Additionally, Stone-Wales defects and vacancies can also contribute to magnetism in graphene. In chemically synthesized graphene, oxygen functionalities predominantly impact magnetism⁶⁰. Processes such as hydrogenation or charge doping have been reported to confer magnetism to graphene⁶¹ albeit often at the expense of compromised electronic behavior⁶². Moreover, magnetism induced by edges, functionalities or non-graphitic doping is extrinsic to graphene lattice, resulting in Curie point far below room temperature⁶³.

Exceeding the threshold limit in graphitic doping holds the potential for pushing the boundaries of magnetism in graphene near room temperature, opening the door for the realization of long-awaited spintronic chips operating at ambient conditions.

Isothermal M vs H measurements (see hysteresis loops in Fig. 6a) were conducted on doped systems, revealing magnetic behavior at room temperature, unlike FLG which is non-magnetic at room temperature (see Fig. S9a, b). Among N-doped samples, NG720 with ultradoping and predominantly graphitic nature; exhibited relatively higher magnetization ~ 4.18 emu⁻¹ compared to NG640 ~ 3.305 emu⁻¹ and NG850 ~ 2.26 emu⁻¹ with lower graphitic content. Similarly, in B-doped samples, BG850 exhibited enhanced magnetization, while BG720, with a lower graphitic extent, showed lower magnetization. Notably, BNG3 displayed higher magnetization and a large coercive field with a mild step in the hysteresis loop, a signature indicative of interface formation between the BN patches and the C lattice. Graphitic doping generally led to increased magnetization, as shown in the magnetization and coercive field results (Fig. 6b). M-H hysteresis loops provided insights into the field training of materials, since a very high field up to ~ 1.4 T is applied, indicating how well they imitate the dictates of magnetic field and retained information upon field withdrawal or reversal.

Each magnetic domain at pyridinic/pyrrolic doped sites responds to the applied field in an isolated manner. However, beyond a certain threshold of dopant incorporation at the graphitic sites, percolation paths formed where spin at each dopant can interact with the other, facilitating the ferromagnetic exchange coupling between dopants. Such spin-spin ferromagnetic exchange-coupling is present in graphitically doped samples, obviating the need for a high external magnetic field for field training. FC-ZFC measurements further explored these dynamics. Predominantly graphitically doped samples like NG720 and BG850 exhibited excellent retrieval, confirming the anticipated exchange coupling. Interestingly, two distinct transition temperatures were registered in graphitically doped samples, $T_{C1} \sim 210$ K and $T_{C2} \sim 330$ K. T_{C1} is the Curie temperature and T_{C2} is the critical ordering temperature. Primarily non-graphitically doped samples displayed larger divergences below transition temperatures, indicating poor spin-spin interactions (see Fig. 6c,d). Additionally, the BG560 sample exhibited mostly paramagnetic behavior in the measurement. Curie Weiss law, expressed as:

$$X = X_0 + \frac{C}{T} \quad (2)$$

C i.e., the slope of inverse of susceptibility vs T plots (see Supplementary Figs 10, 11, 14) revealed insight in to spin-ordering and are sensitive to phase transitions. Thus, peaks in $1/X$ vs. T signify transition temperatures; for instance, NG640 exhibited peaks at ~ 210 , ~ 250 and ~ 320 K, suggesting several competing orderings in NG640. The slope change from negative to positive is a clear indication of phase transition around 210 K. In contrast, NG720 lacks such undesirable competing ordering behavior and remains ferromagnetic up to 400 K. Akin to NG640, BG720 exhibits competing orders and a diamagnetic to ferromagnetic transition around ~ 120 K, whereas BG850 resembles NG720 due to its higher graphitic content. Further transition temperature trends with dopant content and graphitic content detailed in Supplementary Fig. 16. In accordance with Ginzburg-Landau mean field theory, the free energy of a ferromagnet can be given by:

$$F(M, T) = -MH + F(0, T) + a_1(T)M^2 + a_2(T)M^4 + \quad (3)$$

If one ignores terms with higher powers of M , at the critical temperature T_c , the M^2 is linear with H/M . M^2 vs H/M plot also called Arrot plot is a valuable tool to quantify magnetic ordering and to evaluate critical temperature. A larger slope in Arrot plot directly confirms greater spontaneous magnetic order. Even though, close to critical temperature there are departures from linearity attributing to spin fluctuations and due to which

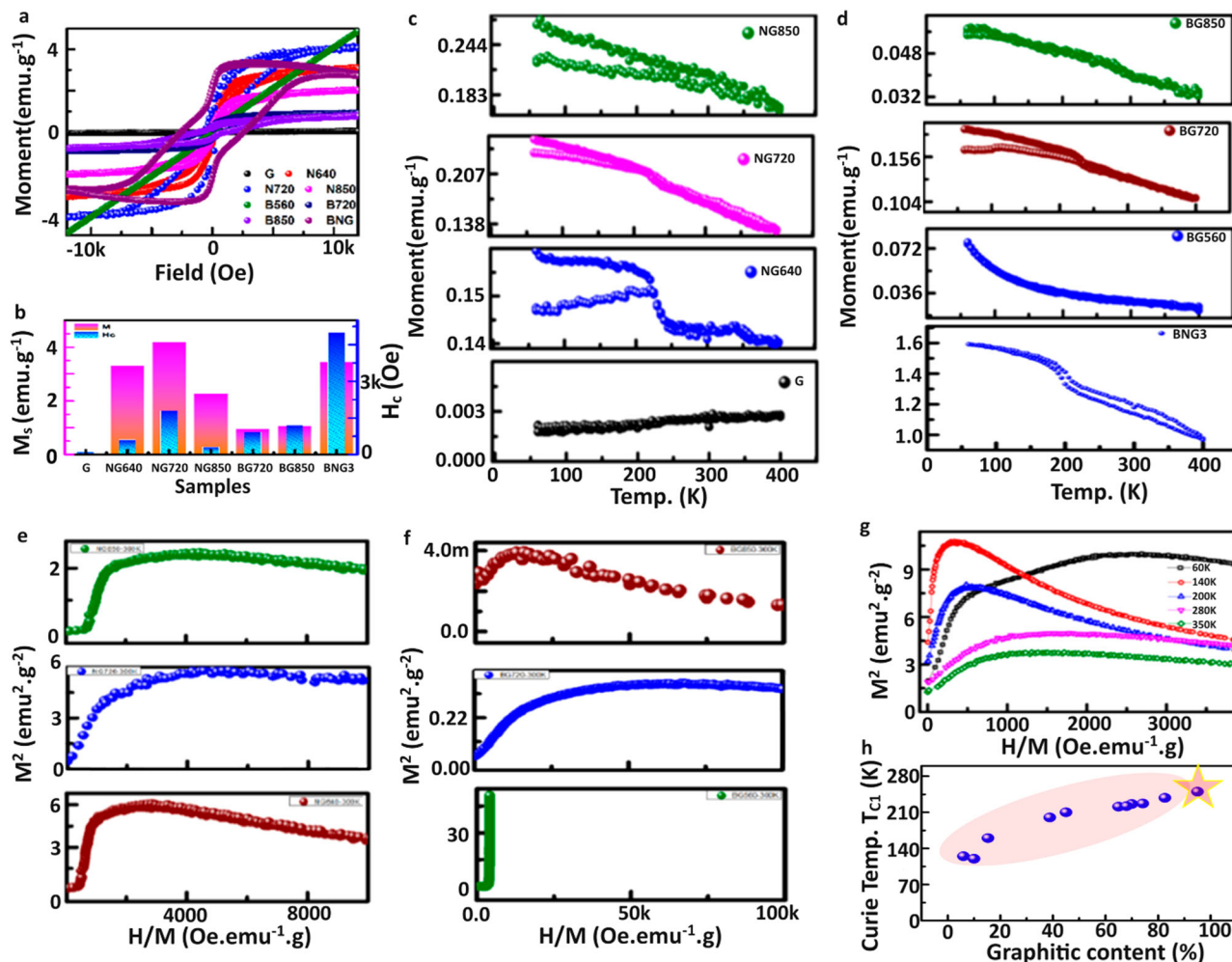


Fig. 6 | Magnetic evolution in doped graphene systems. **a** Isothermal magnetic hysteresis loop for pristine and doped graphene systems at 300 K, **(b)** Histogram plot depicting saturation magnetization and coercive field values for pristine and doped graphene system. Temperature evolution of magnetization behavior evaluated by FC/ZFC plot of **(c)** N-doped samples, **(d)** B-doped samples at various microwave

power and B-, N- co-doped sample BNG3. Room temperature Arrot plot M^2 vs H/M for doped graphene systems **(e)** N-doped systems, **(f)** B-doped systems at various microwave power irradiation, and **(g)** arrot plot for BNG3 at various temperatures. **h** Trend in Curie temperature T_{C1} with graphitic nature of doping in doped samples.

M^4 term becomes crucial^{64,65}. Weak ferromagnets usually follow the linear relationship. Arrot plot of doped samples analyzed for temperature range 60 K to 350 K, revealed a higher spontaneous magnetization in non-graphetically doped samples whereas, NG720, BG850, and BNG3 exhibited curves crossing origin both at room temperature and low temperature, which infers superior room temperature magnetic behavior (see Fig. 6e–g) and Supplementary Figs 12–13 for N-, B- and co-doped samples at room temperature and low temperature. While the presence of a paramagnetic center enhances the saturation magnetization in non-graphitic doped samples, the graphitic motif in graphene lattice provides a pathway for conduction band interaction which strengthens the long-range magnetic ordering (see schematic explanation in Supplementary Fig. 15).

In doped graphene samples two synergistic phenomena, the doping threshold level, and the graphitic percentage bring the transition temperature towards room temperature. Notably, the graphitic motif in graphene lattice facilitates conduction band interaction, fortifying long-range magnetic ordering, as confirmed by Arrot plot analysis. Notably, uncompensated strain serves as an effective means to control and tune magnetism in graphene, but alone it cannot induce ferromagnetism at room temperature. Edge-doping compensated the compressive and tensile strain in low MW power samples exhibiting paramagnetic trends from the local electron-spin imbalance at the edges. Ultimate graphitic overdoping facilitates a spin percolation path elevating the critical temperature T_c towards room temperature. While the non-

graphitic doping bestows extrinsic magnetism and poor magnetic reversal, inherent magnetism generated in graphetically doped samples in contrast exhibited excellent magnetization retrieval and bestowed a high Curie point (see trend in Fig. 6h). While the extrinsic magnetism caused by non-graphitic doping exhibits no signature of magnetization reversal, inherent magnetism generated in graphetically doped samples exhibited excellent magnetization retrieval and bestowed a high Curie point. The interconnected percolative magnetic domains in ultimate graphitic doped samples contribute to bringing magnetic ordering close to 330 K. Additionally, the charge carrier of heteroatom dopants mediates RKKY interaction through conduction band electron. Larger uncompensated strain in BNG samples at the BN patch interface, as evidenced by mechanically strained optical (Supplementary Fig. 2) and HRTEM imaging, facilitates delocalized electrons resulting in strong spin-spin ferromagnetic exchange coupling. Therefore, the combinatorial effect of doping concentration, doping sites, and uncompensated strain in a doped graphene system leads to room-temperature magnetism in otherwise non-magnetic graphene. As indicated by TGA measurements of doped samples (see Supplementary Fig. 8), the doped samples are fairly stable at room temperature and beyond.

In summary, the present report’s ground-breaking discovery reveals that microwave exposure can intelligently facilitate ultimate doping up to theoretical limit, offering intriguing possibilities for potential spintronic application. We achieved the highest possible N-doping level in graphene,

with around 95% of it being graphitic. Similarly, the ever-highest B-doping level of ~19.8% was accomplished. Several unexplored BCN phases have also been synthesized. Microwave doping proves to be a facile, one-pot synthesis method that is reproducible, scalable, fast, green i.e. no catalyst needed, and highly tunable with microwave power acting as the versatile control knob. Our findings represent an experimental breakthrough, pushing the boundaries of doping graphene toward the theoretical limit. While retaining electronic mobility, the primarily graphitic doped samples exhibited excellent carrier concentration $\sim 9.2 \times 10^{12} \text{ cm}^{-2}$. Inherent magnetism in graphetically doped systems exhibited excellent magnetization retrieval and bestowed a high Curie point, which would help in inching towards room temperature spintronic chips made up of doped graphene systems, which has remained a rare dream for quite a while. Achieving the highest graphitic doping not only allows controlled carrier injection into graphene, retaining carrier mobility but also leads to phase stability and access to unexplored physics, including Dirac behavior even at elevated temperatures, a phenomenon previously exclusive to low temperatures, and the evolution of new quantum states. Furthermore, graphetically doped graphene holds promise for emerging applications in fast electronics (THz)⁶⁶, in excitonics⁶⁷, and as catalysts⁶⁸. In conclusion, the present work marks a breakthrough in graphene research, paving the way for challenging technological applications and opening new dimensions in the years to come.

Methods

Synthesis of samples

There are several control parameters in the doping reaction of graphene such as microwave parameters (microwave power, exposure time etc), precursor materials (microwave activity), solvents etc (high microwave absorption). We kept a cylindrical reaction vessel at the center of the microwave oven tray, as the local electric field is maximum in the central region. The vessel was intentionally kept closed during reaction so that fluid being heated generates pressure inside the vessel which possibly would catalyze the reaction. Dielectric constants of precursors and solvents decide the electric field pattern inside the microwave oven, and therefore the choice has to be made judiciously. Moreover, the choice of solvents is very crucial as it needs to disperse precursors, help focus microwave energy and at the same time it should not degrade itself under microwave exposure or catch fire under exposure. We investigated several solvents and several nitrogen and boron precursors and finally we carried out detailed experiments with IPA as solvent and NH_4OH and B_2O_3 as precursors for N and B respectively.

Precursors used are few layered graphene (United Nanotech Innovations), precursor for N-dopant and B-dopant are ammonia and B_2O_3 (both sigma Aldrich with 99.99% purity). The solution containing graphene and doping precursor, was made by taking 0.5–1: 0.4–1.5 ratio of doping precursor in 10–100 ml of solvent (IPA). This mixture was sonicated in an ultrasonicator for 1–2 h to obtain a fully dispersed solution. The amount of solvent taken in the microwave vessel was kept intentionally 10% of the total volume, this was to avoid any undesirable spill of the solvent which has low ignition point and may catch fire. Exposure of microwave was in shots of 1 min (total 5–10 shots) and the generated pressure was frequently released. After natural cooling to the room temperature, the above samples were centrifuged with DI water, IPA and ethanol few times. After centrifugation for optimized duration and at optimized rpm, the samples were dried. Boron and nitrogen co-doped samples were synthesized by varying the nitrogen and boron precursor ratio (0.5–1: 0.4–1.5) while keeping the power of the microwave fixed at 720 W. Power and the irradiation time in the microwave synthesis method was varied in speculation of getting a better doping level.

Computational details

We have used spin-polarized density functional theory (DFT) methods as implemented in the SIESTA package with PBE exchange-correlation functional^{26,27} to calculate all the electronic properties. We have used 4×4 supercells for all the calculations (see Supplementary Fig 3). We have used a vacuum of 20 Angstrom in the non-periodic direction to avoid any

unwanted interactions. We have sampled the Brillouin Zone with $15 \times 15 \times 1$ K points for all the calculations. All the systems are relaxed until the force per atom is reduced to 0.02 eV/Angstrom.

Characterizations

We have characterized the crystalline qualities of our doped samples employing X-ray diffraction, High Resolution Transmission Electron Microscopy (HRTEM) and Selected Area Electron Diffraction (SAED). To investigate the remaining functional groups attached to the surface of graphene, Fourier Transform Infrared Spectroscopy (FTIR) was used. To examine the thermal stability of graphene samples when undergoing through doping reaction, we have carried out Thermal Gravimetric Analysis (TGA). To identify molecular fingerprints and to evaluate number of layers in doped graphene sheets Raman spectroscopy was carried out. It also evaluates defects present in the system. X-ray Photoelectron Spectroscopy (XPS) was carried out to further pinpoint on doping in order to quantify doping level and to know different types of doping present in doped graphene systems.

The Raman spectroscopy for pristine graphene and doped graphene has recorded in the range of $300\text{--}3000 \text{ cm}^{-1}$ in the back scattering mode using Micro-Raman spectrometer with 532 nm laser as excitation source by STR Raman Spectrograph. A 100x magnification optical microscope from Olympus was used to focus and collect the light. The optical imaging of doped samples was done employing Olympus microscope integrated with confocal Micro-Raman Spectrometer.

The thermal stability of pristine graphene and doped graphene were analyzed on TGA analyzer (STA 6000, Perkin Elmar USA) under oxygen ambience. FTIR spectra for all samples have been recorded on Shimadzu IrAfinity-1. TEM from JEOL (JEM 2100) was used for imaging (TEM, HRTEM and SAED) for graphene and doped samples. Titan Themis 300 kV from FEI was used for atomically resolved images (TEM, Atomic TEM and SAED) for G, NG720, BG720 and BNG3. Atomic percentages have been calculated from XPS data (acquired in ESCA+ Omicron Nanotechnology GmbH under an ultrahigh vacuum level).

Fabrication of FET and measurements

In order to investigate the field effect, an FET device was fabricated employing extreme UV mask-photolithography and Au/Ti metallization by e-beam evaporation to have a final device having a channel length of $\sim 0.5 \mu\text{m}$ and a channel width of $10 \mu\text{m}$ over 100 nm of thermally oxidized silicon surface on silicon substrate. The influence of gate voltage on in-plane (i.e., drain to source) conductivity has been investigated for G, NG, BG and BNG samples. To determine carrier concentration, carrier mobility, n-type and p-type behavior (i.e., Electrical characterization) we carried out FET device measurements (for NG720, BG720 and BNG3) by investigating its output i.e., and transfer characteristics. Mobility values were calculated from

$$\mu = \frac{L}{W} C_G V_{DS} \left(\frac{\Delta I_{SD}}{\Delta V_G} \right) \quad (4)$$

where L is the channel length, W is its width, C_G is the capacitance per unit area. Electron and hole mobility have been determined from slopes of the transfer characteristic from segments right and left of the Dirac point respectively. Experimentally, net majority carrier concentration can be attained by monitoring Dirac Voltage.

$$\Delta n = \frac{C_i}{q} (\Delta V_D) \quad (5)$$

Where Δn is net majority carrier concentration, c_i is the capacitance per unit area of the oxide layer.

Magnetic behavior analysis

In order to evaluate the magnetic behavior of doped graphene system, a vibrating sample measurement (VSM) instrument from Quantum Design Versa Lab has been utilized. The temperature evaluation of magnetic

behavior has been recorded from 60 to 400 K in the sweep mode. Zero fields cooled magnetization vs temperature (MT) has been recorded without applying any dictating field however, field-cooled MT is recorded at very low field of 100 Oe. Isothermal magnetic hysteresis loops are recorded in vicinity of static external magnetic field in range varying from -3 T to 3 T at different temperature values below and above transition temperature. Magnetization values were corrected assuming the response of the sample holder.

Data availability

Data is available in electronic supplementary information.

Received: 28 May 2023; Accepted: 28 February 2024;

Published online: 08 March 2024

References

- Novoselov, K. S. et al. Electric field effect in atomically thin carbon films. *Science* **306**, 666–669 (2004).
- Geim, A. K. & Novoselov, K. S. The rise of graphene. *Nat. Mater.* **6**, 183–191 (2007).
- Ranjan, P. et al. 2D materials: increscent quantum flatland with immense potential for applications. *Nano Convergence* **9**, 26 (2022).
- Motlag, M. et al. Asymmetric 3D elastic–plastic strain-modulated electron energy structure in monolayer graphene by laser shocking. *Adv. Mater.* **31**, 1900597 (2019).
- Chahal, S. et al. Microwave nanoarchitectonics of black phosphorene for energy storage. *Matter* **7**, 237–254 (2024).
- Vogt, P. et al. Compelling experimental evidence for graphene like two-dimensional silicon. *Phys. Rev. Lett.* **108**, 155501 (2012).
- Mannix, A. J. et al. Synthesis of borophenes: Anisotropic, two-dimensional boron polymorphs. *Science* **350**, 1513–1516 (2015).
- Ranjan, P. et al. Freestanding borophene and its hybrids. *Adv. Mater.* **31**, 1900353 (2019).
- Ranjan, P., Lee, J. M., Kumar, P. & Vinu, A. Borophene: New sensation in flatland. *Adv. Mater.* **32**, 2000531 (2020).
- Chahal, S. et al. Borophene via micromechanical exfoliation. *Adv. Mater.* **33**, 2102039 (2021).
- Vishwakarma, K. et al. Quantum coupled borophene based heterolayers for excitonic and molecular sensing applications. *Phys. Chem. Chem. Phys.* **24**, 12816 (2022).
- Chahal, S., Bandyopadhyay, A., Dash, S. P. & Kumar, P. Microwave synthesized 2d gold and its 2D-2D hybrids. *J. Phys. Chem. Lett.* **13**, 6487–6495 (2022).
- Chahal, S. et al. Beryllene, the lightest Xene. *npj 2D Mater. Appl.* **7**, 55 (2023).
- Sahu, T. K. et al. Microwave synthesis of molybdenene from MoS₂. *Nat. Nanotechnol.* **18**, 1430–1438 (2023).
- Rao, C. N. R. et al. A study of the synthetic methods and properties of graphenes. *Sci. Technol. Adv. Mater.* **11**, 054502 (2010).
- Molle, A. et al. Buckled two-dimensional Xene sheets. *Nat. Mater.* **16**, 163–169 (2017).
- Chaves, A. et al. Bandgap engineering of two-dimensional semiconductor materials. *npj 2D Mater. Appl.* **4**, 29 (2020).
- Chahal, S., Kauzlarich, S. M. & Kumar, P. Microwave synthesis of hematene and other two-dimensional oxides. *ACS Mater. Lett.* **3**, 631–640 (2021).
- Li, X. et al. MXene chemistry, electrochemistry and energy storage applications. *Nat. Rev. Chem.* **6**, 389–404 (2022).
- Subrahmanyam, K. S. et al. Chemical storage of hydrogen in few-layer graphene. *Proc. Natl Acad. Sci.* **108**, 2674–2677 (2011).
- Gopalakrishnan, K., Subrahmanyam, K. S., Kumar, P., Govindaraj, A. & Rao, C. N. R. Reversible chemical storage of halogens in few-layer graphene. *RSC Adv.* **2**, 1605–1608 (2012).
- Kumar, P. et al. Photoluminescence, white light emitting properties and related aspects of ZnO nanoparticles admixed with graphene and GaN. *Nanotechnology* **21**, 385701 (2010).
- Liu, J., Kumar, P., Hu, Y., Cheng, G. J. & Irudayaraj, J. Enhanced multiphoton emission from CdTe/ZnS quantum dots decorated on single-layer graphene. *J. Phys. Chem. C.* **119**, 6331–6336 (2015).
- Das, S. R. et al. Single-layer graphene as a barrier layer for intense uv laser-induced damages for silver nanowire network. *ACS Nano* **9**, 11121–11133 (2015).
- Kumar, P., Nian, Q., Xiong, G., Fisher, T. S. & Cheng, G. J. Laser engineering of heterostructured graphitic petals on carbon nanotubes forests for robust thermal interface capable of swift heat transfer. *Mater. Adv.* **4**, 2402–2409 (2023).
- Lee, S., Kumar, P., Hu, Y., Cheng, G. J. & Irudayaraj, J. Graphene laminated gold bipyramids as sensitive detection platforms for antibiotic molecules. *Chem. Commun.* **51**, 15494–15497 (2015).
- Hu, Y. et al. Water flattens graphene wrinkles: laser shock wrapping of graphene onto substrate-supported crystalline plasmonic nanoparticle arrays. *Nanoscale* **7**, 19885–19893 (2015).
- Kumar, P. et al. Laser shock tuning dynamic interlayer coupling in graphene–boron nitride moiré superlattices. *Nano Lett.* **19**, 283–291 (2019).
- Han, W., Kawakami, R. K., Gmitra, M. & Fabian, J. Graphene spintronics. *Nat. Nanotechnol.* **9**, 794–807 (2014).
- Lin, L. et al. Nitrogen cluster doping for high-mobility/conductivity graphene films with millimeter-sized domains. *Sci. Adv.* **5**, eaaw8337 (2019).
- Błoński, P. et al. Doping with graphitic nitrogen triggers ferromagnetism in graphene. *J. Am. Chem. Soc.* **139**, 3171–3180 (2017).
- Wang, X. et al. Doping of graphene through electrothermal reactions with ammonia. *Science* **324**, 768–771 (2009).
- Li, J. et al. Searching for magnetism in pyrrolic N-doped graphene synthesized via hydrothermal reaction. *Carbon* **84**, 460–468 (2015).
- Bhushan, R., Kumar, P. & Thakur, A. K. Catalyst-free solvothermal synthesis of ultrapure elemental N- and B- doped graphene for energy storage application. *Solid State Ion.* **353**, 115371 (2020).
- Liu, Y. et al. Elemental super doping of graphene and carbon nanotubes. *Nat. Commun.* **7**, 10921 (2016).
- Wang, H., Maiyalagan, T. & Wang, X. Review on Recent Progress in Nitrogen-doped graphene: synthesis, characterization, and its potential applications. *ACS Catalysis* **2**, 781–794 (2012).
- Boas, C. R. S. V. et al. Characterization of nitrogen doped graphene bilayers synthesized by fast, low temperature microwave plasma-enhanced chemical vapour deposition. *Sci. Rep.* **9**, 13715 (2019).
- Kumar, P., Yamijala, S. S. R. K. C. & Pati, S. K. Optical unzipping of carbon nanotubes in liquid media. *J. Phys. Chem. C.* **120**, 16985–16993 (2016).
- Panchakarla, L. S. et al. Synthesis, structure, and properties of boron- and nitrogen-doped graphene. *Adv. Mater.* **21**, 4726–4730 (2009).
- Wang, X. et al. Heteroatom-doped graphene materials: syntheses, properties and applications. *Chem. Soc. Rev.* **43**, 7067–7098 (2014).
- Chahal, S. et al. Microwave flash synthesis of phosphorus and sulphur ultradoped graphene. *Chem. Eng. J.* **450**, 138447 (2022).
- Li, Z. et al. Small <https://doi.org/10.1002/sml.202307610> (2024).
- Dhanasekaran, R. & Ramasamy, P. Effect of an external electric field on two-dimensional nucleation. *Il Nuovo Cim. D.* **7**, 506–512 (1986).
- Kumar, P., Krishna, M. G. & Bhattacharya, A. K. Electric-field-induced nanostructuring of metallic thin films. *Int. J. Nanosci.* **7**, 255–261 (2008).
- Mai, H. L., Cui, X.-Y., Stampfl, C. & Ringer, S. P. The role of vacancies in electric field mediated graphene oxide reduction. *Appl. Phys. Lett.* **113**, 073103 (2018).
- Wang, Y. et al. Room-temperature ferromagnetism of graphene. *Nano Lett.* **9**, 220–224 (2009).
- Shi, Z., Kutana, A. & Yakobson, B. I. How much N-Doping can graphene sustain? *J. Phys. Chem. Lett.* **6**, 106–112 (2015).
- Wang, X., Christopher, J. W. & Swan, A. K. 2D Raman band splitting in graphene: Charge screening and lifting of the K-point Kohn anomaly. *Sci. Rep.* **7**, 13539 (2017).

49. Ferrari, A. C. et al. Raman spectrum of graphene and graphene layers. *Phys. Rev. Lett.* **97**, 187401 (2006).
50. Terrones, H., Lv, R., Terrones, M. & Dresselhaus, M. S. The role of defects and doping in 2D graphene sheets and 1D nanoribbons. *Rep. Prog. Phys.* **75**, 062501 (2012).
51. Wang, S. et al. BCN graphene as efficient metal-free electrocatalyst for the oxygen reduction reaction. *Angew. Chem. Int. Ed.* **51**, 4209–4212 (2012).
52. Heisenberg, W. Zur Theorie des ferromagnetismus. *Z. F., Phys.* **49**, 619–636 (1928).
53. Slater, J. C. Ferromagnetism, and the band theory. *Rev. Mod. Phys.* **25**, 199–210 (1953).
54. Stoner, E. C. Ferromagnetism. *Rep. Prog. Phys.* **11**, 304 (1947).
55. Wohlfarth, E. P. The theoretical and experimental status of the collective electron theory of ferromagnetism. *Rev. Mod. Phys.* **25**, 211–219 (1953).
56. Kittel, C., Introduction to solid state physics (7th ed.). New York [u.a.]: Wiley. ISBN 978-0471111818 (1996).
57. Capellmann, H. Theory of itinerant ferromagnetism in the 3-d transition metals. *Z. Phys. B Condens. Matter Quanta* **34**, 29–35 (1979).
58. Sepioni, M., Nair, R. R., Tsai, I.-L., Geim, A. K. & Grigorieva, I. V. Revealing common artifacts due to ferromagnetic inclusions in highly oriented pyrolytic graphite. *Europhys. Lett.* **97**, 47001 (2012).
59. Tuček, J. et al. Emerging chemical strategies for imprinting magnetism in graphene and related 2D materials for spintronic and biomedical applications. *Chem. Soc. Rev.* **47**, 3899–3990 (2018).
60. Liu, Y. et al. Realization of ferromagnetic graphene oxide with high magnetization by doping graphene oxide with nitrogen. *Sci. Rep.* **3**, 2566 (2013).
61. García-Martínez, N. A., Lado, J. L., Jacob, D. & Fernández-Rossier, J. Anomalous magnetism in hydrogenated graphene. *Phys. Rev. B* **96**, 024403 (2017).
62. Zhang, J. et al. Tunable electronic properties of graphene through controlling bonding configurations of doped nitrogen atoms. *Sci. Rep.* **6**, 28330 (2016).
63. Kabir, M. & Saha-Dasgupta, T. Manipulation of edge magnetism in hexagonal graphene nanoflakes. *Phys. Rev. B* **90**, 035403 (2014).
64. Zhang, Y. et al. Arrott plots, M^4 plots and the critical temperature of the weak ferromagnet $\text{FeGa}_{3-y}\text{Ge}_y$. *AIP Adv.* **8**, 101429 (2018).
65. Murata, K. K. & Doniach, S. Theory of magnetic fluctuations in itinerant ferromagnets. *Phys. Rev. Lett.* **29**, 285–288 (1972).
66. Tassin, P., Koschny, T. & Soukoulis, C. M. Graphene for terahertz applications. *Science* **341**, 620–621 (2013).
67. Johannsen, J. C. et al. Tunable carrier multiplication and cooling in graphene. *Nano Lett.* **15**, 326–331 (2015).
68. Wu, J. et al. A metal-free electrocatalyst for carbon dioxide reduction to multi-carbon hydrocarbons and oxygenates. *Nat. Commun.* **7**, 13869 (2016).
69. Tao, L. et al. Silicene field-effect transistors operating at room temperature. *Nat. Nanotechnol.* **10**, 227–231 (2015).
70. Guo, B. et al. Controllable N-doping of graphene. *Nano Lett.* **10**, 4975–4980 (2010).
71. Hwang, W. S. et al. Graphene nanoribbon field-effect transistors on wafer-scale epitaxial graphene on SiC substrates. *APL Mater.* **3**, 011101 (2015).
72. Lu, Y.-F. et al. Nitrogen-doped graphene sheets grown by chemical vapor deposition: synthesis and influence of nitrogen impurities on carrier transport. *ACS Nano* **7**, 6522–6532 (2013).
73. Wang, G. et al. Seamless lateral graphene p–n junctions formed by selective in situ doping for high-performance photodetectors. *Nat. Commun.* **9**, 5168 (2018).
74. Chen, H. et al. Experimental demonstration of microwave absorber using large-area multilayer graphene-based frequency selective surface. *IEEE Trans. Microw. Theory Tech.* **66**, 3807–3816 (2018).

Acknowledgements

We acknowledge the Indian Institute of Technology Patna for experimental facilities. PK acknowledges the Department of Science and Technology, Govt. of India, for a Research grant under the Ramanujan Fellowship (Sanction No. SB/S2/RJN-205/2014).

Author contributions

PK conceived the idea. RB carried out microwave doping of graphene and characterized the samples. SK helped with FET characterization. AB carried out density functional theory calculations for doped graphene systems. Results were discussed with SKP and AKT. RB and PK wrote the manuscript together. The project was finished under the supervision of PK.

Competing interests

The authors declare no competing interests.

Additional information

Supplementary information The online version contains supplementary material available at <https://doi.org/10.1038/s41699-024-00457-w>.

Correspondence and requests for materials should be addressed to Prashant Kumar.

Reprints and permissions information is available at <http://www.nature.com/reprints>

Publisher's note Springer Nature remains neutral with regard to jurisdictional claims in published maps and institutional affiliations.

Open Access This article is licensed under a Creative Commons Attribution 4.0 International License, which permits use, sharing, adaptation, distribution and reproduction in any medium or format, as long as you give appropriate credit to the original author(s) and the source, provide a link to the Creative Commons licence, and indicate if changes were made. The images or other third party material in this article are included in the article's Creative Commons licence, unless indicated otherwise in a credit line to the material. If material is not included in the article's Creative Commons licence and your intended use is not permitted by statutory regulation or exceeds the permitted use, you will need to obtain permission directly from the copyright holder. To view a copy of this licence, visit <http://creativecommons.org/licenses/by/4.0/>.

© The Author(s) 2024